AGU PUBLICATIONS

JGR

Journal of Geophysical Research: Oceans

RESEARCH ARTICLE

10.1002/2013JC009662

Key Points:
- Recovery of oceanic T, S, and potential density from acoustic reflectivity data
- Thermal anomalies observations at the Mediterranean tongue level
- Comparison between acoustic reflectors in the ocean and isopycnals

Supporting Information:
- Methods
- Supporting figures

Correspondence to:
B. Biescas,
biescas@icm.csic.es

Citation:
Biescas, B., B. R. Ruddick, M. R. Nedimovic, V. Sallarès, G. Bornstein, and J. F. Mojica (2014), Recovery of temperature, salinity, and potential density from ocean reflectivity, *J. Geophys. Res. Oceans*, *119*, 3171–3184, doi:10.1002/2013JC009662.

Received 28 NOV 2013
Accepted 5 MAY 2014
Accepted article online 10 MAY 2014
Published online 29 MAY 2014

Recovery of temperature, salinity, and potential density from ocean reflectivity

Berta Biescas[1,2], Barry R. Ruddick[1], Mladen R. Nedimovic[3,4,5], Valentí Sallarès[2], Guillermo Bornstein[2], and Jhon F. Mojica[2]

[1]Department of Oceanography, Dalhousie University, Halifax, Nova Scotia, Canada, [2]Department of Marine Geology, Institut de Ciències del Mar ICM-CSIC, Barcelona, Spain, [3]Department of Earth's Sciences, Dalhousie University, Halifax, Nova Scotia, Canada, [4]Lamont-Doherty Earth Observatory of Columbia University, Palisades, New York, USA, [5]University of Texas Institute for Geophysics, Austin, Texas, USA

Abstract This work explores a method to recover temperature, salinity, and potential density of the ocean using acoustic reflectivity data and time and space coincident expendable bathythermographs (XBT). The acoustically derived (vertical frequency >10 Hz) and the XBT-derived (vertical frequency <10 Hz) impedances are summed in the time domain to form impedance profiles. Temperature (T) and salinity (S) are then calculated from impedance using the international thermodynamics equations of seawater (GSW TEOS-10) and an empirical T-S relation derived with neural networks; and finally potential density (ρ) is calculated from T and S. The main difference between this method and previous inversion works done from real multichannel seismic reflection (MCS) data recorded in the ocean, is that it inverts density and it does not consider this magnitude constant along the profile, either in vertical or lateral dimension. We successfully test this method on MCS data collected in the Gulf of Cadiz (NE Atlantic Ocean). T, S, and ρ are inverted with accuracies of $\delta T_{sd}=0.1^{\circ}$C, $\delta S_{sd}=0.09$, and $\delta\rho_{sd}=0.02$kg/m^3. Inverted temperature anomalies reveal baroclinic thermohaline fronts with intrusions. The observations support a mix of thermohaline features created by both double-diffusive and isopycnal stirring mechanisms. Our results show that reflectivity is primarily caused by thermal gradients but acoustic reflectors are not isopycnal in all domains.

1. Introduction

Temperature, salinity, and potential density of oceanic mesoscale and submesoscale subsurface structure are traditionally measured with vertical profilers such as expendable bathythermographs (XBT) or conductivity-temperature profilers (CTD), which provide data at a resolution that is typically three orders of magnitude higher in the vertical ($\sim$1 m) than in the horizontal ($\sim$1 km) dimension. Seismic oceanography (SO) is a scientific discipline that is applied to investigate the ocean using acoustic reflectivity data collected with multichannel seismic (MCS) systems, which were originally designed for solid earth studies and applied for the first time to the water layer by *Gonella and Michon* [1988] and *Holbrook et al.* [2003]. This acoustic method can sample lateral sections of hundreds of kilometers to full ocean depth, with resolutions of $\sim 10-100$ m and $\sim$10 m in lateral and vertical dimensions, respectively.

A topic attracting increasing interest in SO is the inversion of oceanic variables from acoustic reflectivity. So far, two studies have been published focusing on the recovery of sound speed, temperature, and salinity from field MCS data. The first one by *Wood et al.* [2008] presents 1-D temperature profiles up to a depth of 750 m that were computed by applying the full waveform inversion. The method reported an accuracy of 0.5°C for the inverted 1-D temperature profiles. The second work is that of *Papenberg et al.* [2010], in which the authors recover 1-D temperature and salinity profiles from MCS data and coincident XBTs and CTDs. *Papenberg et al.* [2010] inverted stacked reflection sections hundreds of kilometers long that sampled up to 1700 m of the water column into temperature and salinity profiles with accuracies of 0.1°C and 0.1, respectively. Recently, two MCS synthetic data studies that detail methodology and show the potential of using full waveform inversion in oceanographic research have been published by *Kormann et al.* [2011] and *Bornstein et al.* [2013].

Temperature and salinity are physical properties that describe structures in the ocean. However, the main physical parameter that controls ocean dynamics is density and, since the ocean is a compressible fluid, potential density is the property that determines the stability, mixing, and mesoscale motions of the

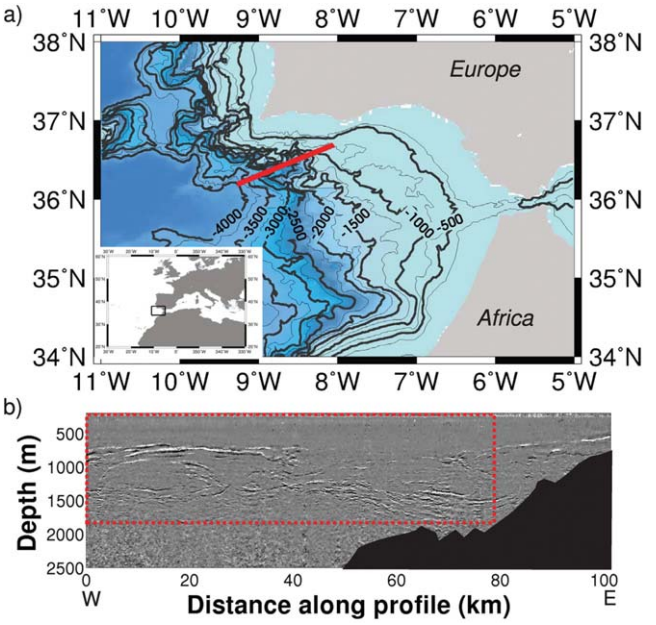

Figure 1. (a) The GOLR01 profile was acquired during the GO Survey in the Gulf of Cadiz, Northeastern Atlantic Ocean, 1 May 2007. The solid red line shows the location of the GOLR01 profile. (b) Multichannel seismic reflection data of the GOLR01 profile. Gray colors scale the amplitude of the acoustic reflectivity. The red square contains the inverted data. The solid black shape shows the bathymetry of the seabed.

particles. This work explores a numerical approach to recovering temperature, salinity, and potential density, from field acoustic reflectivity data. The used inversion method is based on the one proposed by *Papenberg et al*. [2010], with two key advances: (i) density is derived from inverted T and S and it is not considered as a constant and (ii) a T-S relation derived using neural networks (NN) is used to retrieve salinity out of temperature. The analyzed MCS data were acquired during the GO Survey, that took place in the Gulf of Cadiz, northeastern Atlantic Ocean in April–May 2007. In this survey, XBT and CTD casts were acquired coincident in time and/or space with the MCS data.

First, the study area and data are briefly described. Next the algorithm used to precondition the MCS data for the inversion and the inversion method itself are presented. This is followed by the description of the method application to the profile GOLR01 to retrieve temperature, salinity, and potential density values. The inverted values are then compared with coincident XBT and CTD data and the errors are estimated. The resulting isopycnals are compared with the imaged acoustic reflectors as well as with the thermohaline anomalies. Finally, the results and possible future directions are discussed.

2. Study Area and Data

The method described in this work has been applied to the MCS profile GOLR01, acquired in the Gulf of Cadiz (NE Atlantic Ocean) during the GO survey (Figure 1). In this area, the Mediterranean Outflow leaves the Strait of Gibraltar and flows into the Atlantic Ocean following the South Iberian margin. The dense overflow descends and reaches a neutral buoyancy at a depth between 600 and 1500 m, where it is called the Mediterranean Undercurrent (MU). The salty and warm MU turns northward, deflected by the Coriolis effect and continues along the continental slope. The MU has an upper core, usually observed between 700 and 800 m and a lower core, at a depth of 1000–1200 m. A substantial fraction of Mediterranean Water (MW) separates from the continental slope and enters the interior North Atlantic, mixing with North Atlantic Intermediate Water (NAIW) and North Atlantic Deep Water (NADW) [*Bower et al*., 2002; *Ambar et al*., 2002; *Buffett et al*., 2009]. The interaction of the MU with abrupt topographic changes of the continental slope, like major canyons or capes, can generate coherent anticyclonic lenses of Mediterranean-origin water called meddies [*Armi et al*., 1989; *Richardson et al*., 2000; *Serra and Ambar*, 2005; *Biescas et al*., 2008]. Thermohaline staircases located at the bottom of the lower core of the MW outflow are observed and described as double-diffusive structures [*Tait and Howe*, 1968; *Ruddick and Richards*, 2003; *Biescas et al*., 2010]. Multiscale observations also describe isopycnal stirring by mesoscale eddies and diapycnal mixing at the MW level [*Ferrari and Polzin*, 2005].

2.1. Acoustic Data

The acoustic reflection data were acquired with a MCS system installed on board the RRS Discovery. The acoustic source consisted of 6 Bolt 1500LL airguns with a total volume of 2320 cu.in. and a peak energy ranging between 10 and 60 Hz. The source array was shot every 20 s (20 m). Reflected energy was recorded using a 2400 m long SERCEL streamer with 192 channels and 12.5 m group spacing. There were 16

hydrophones spaced at 0.625 m in each receiver group. The streamer was deployed 84 m away from the acoustic source, at a depth of 8 m. The source and the streamer were towed from the port side to leave the starboard side free for deployment of the oceanographic probes.

2.2. Oceanographic Data

Thirty-two Lockheed Martin Sippican expendable bathythermographs (XBT-T5), coincident in time and space to the acoustic acquisition, were deployed from RRS Discovery along the GOLR01 profile. XBTs reached depths of 1830 m and were deployed every ~2.5 km (Figure 5a), which is the maximum lateral resolution that can be achieved using only one XBT recording system on board and taking into account the time needed for the probes to drop to 1830 m. The sound speed data from the XBT files were not used in this work, since these values are calculated using a constant default salinity of 35 psu. Four CTD casts were made (Figure 5a), with a lateral sampling of ~20 km, along the profile. These casts were done from FS Poseidon 2–3 h after the acoustic data acquisition. CTD deployment could not be done from the vessel that acquired the acoustic data because CTD cast deployment requires stopping the vessel, while the MCS system needs continuous movement of the vessel to maintain the depth control of the streamer.

3. Methodology

3.1. Data Preconditioning

The inversion process described in this study is highly sensitive to the quality and accuracy of the collected input acoustic data. Preserving true amplitudes and enhancing the signal-to-noise ratio (*S*/*N*) of acoustic data are one of the standard goals of MCS data processing but are of particular importance in SO studies because reflectivity in the ocean is $\sim 10^3$ times weaker than in the solid earth. The data preconditioning approach developed in this work consists of several steps that transform the input raw shot gather into profiles of zero-offset true-amplitude acoustic reflectivity (*R* from here on) in the water layer. Detailed information is provided about the data preconditioning steps that are specific to this work. Standard MCS data processing steps [see *Yilmaz*, 2001] are only listed.

The main steps of the first part of the method are detailed here:

1. *Geometry*. Developed and applied nominal 2-D geometry to data headers.

2. Amplitude corrections:

2.1. *Angle of incidence*. Angle of incidence correction is of particular importance in SO investigations because the ratio between the maximum source-receiver offset and the average target reflector depth for these studies is greater than in any other MCS reflection application. This means that the incident angle for water layer reflections and, therefore, the reflection amplitude from the same subsurface locations in common midpoint (CMP) gathers strongly vary with the changing source-receiver offset (Figure 2a). The amplitude variation with angle of incidence is computed using Zoeppritz's equations [e.g., *Sheriff and Geldart*, 1982] and removed for all nonzero-offset data, which usually is all of the collected data, to produce a true-amplitude zero-offset reflection section, as follows:

$$R(\theta)=R(0)+G\sin^2(\theta)+F(\tan^2(\theta)-\sin^2(\theta)), \tag{1}$$

where θ is the incidence angle, which will vary with depth and receiver. For a liquid acoustic medium R(0),G and F are given by:

$$R(0)=\frac{1}{2}\left(\frac{\Delta V_P}{V_P}+\frac{\Delta\rho}{\rho}\right), \tag{2}$$

$$G=\frac{1}{2}\frac{\Delta V_P}{V_P}, \tag{3}$$

$$F=\frac{1}{2}\frac{\Delta V_P}{V_P}, \tag{4}$$

where V_P is sound speed, ρ is density, and Δ means variation. To correct *R* to normal incidence, we apply the factor $GainZoep=\frac{R(0)}{R(\theta)}$ (Figure 2b). In our data, $\frac{\Delta\rho}{\rho}\ll\frac{\Delta V_P}{V_P}$ for a layer with a thickness of ~10 m, which is

the vertical resolution of the acoustic reflection data. Hence, using equations (1) and (2), we get the correction that is applied to every shot gather as a matrix factor for all depths and receivers:

$$GainZoep = \frac{1}{1+\tan^2(\theta)} \tag{5}$$

2.2. *Receiver directivity*. Directivity correction removes amplitude variations due to the receiver array response. Data traces recorded on each channel of the MCS streamer represent a combined recording of a group of hydrophones (16 in this study) distributed over the group interval. The directivity correction is calculated from the following equation [*Sheriff and Geldart*, 1982]:

$$GainIns = abs\left[\frac{\sin\left(nr * \frac{\pi * \Delta x}{\lambda} * \left(\sin\left(atan(\theta)\right)\right)\right.}{nr * \sin\left(\frac{\pi * \Delta x}{\lambda} * \sin\left(atan(\theta)\right)\right.}\right], \tag{6}$$

where θ is the incidence angle, nr is the number of hydrophones that generated the signal of data trace corresponding to a particular channel, λ is the wavelength of the peak energy of the source, and Δx is the distance between the hydrophones that are stacked to generate one channel. *GainIns* is calculated as a matrix of coefficients and applied to each shot gather (Figure 2c).

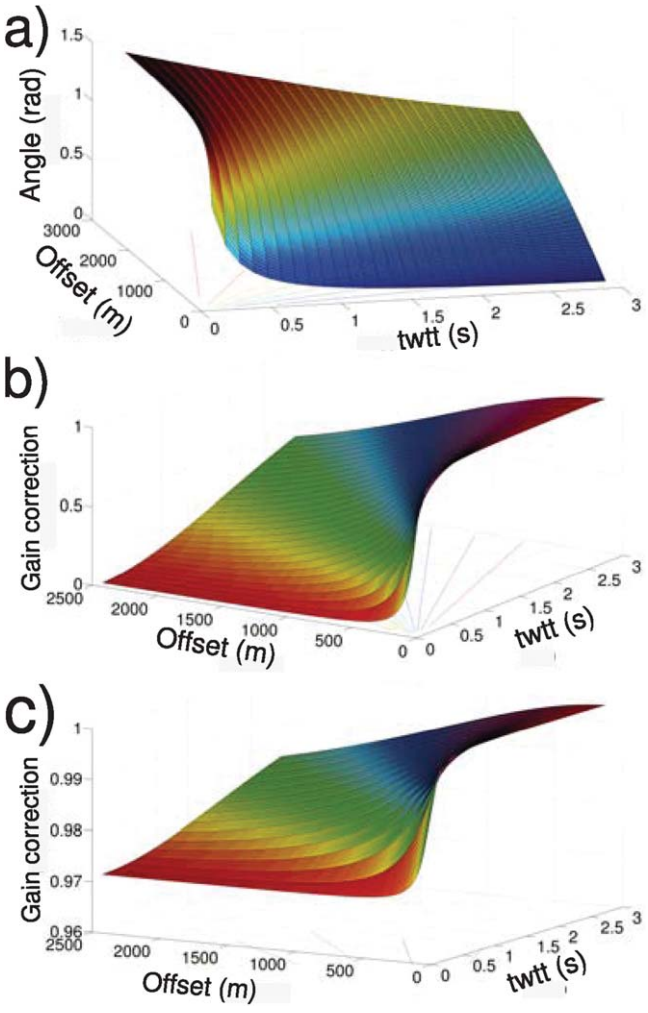

Figure 2. (a) Variation of the incident angle with distance between source and receivers (offsets) and recorded two-way travel time (twtt) of reflections. Note that most of the ocean reflectivity is confined to the top 2 km of the water column or ~3*s* twtt. (b) GainZoep amplitude factor applied to compensate reflectivity to normal incidence (equation (5)). (c) Amplitude factor applied to correct the array response (equation (6)).

2.3. Amplitude correction for spherical divergence.

3. *Band-pass frequency filter* of [10–80] Hz to remove noise.

4. *LIFT filtering*. We have applied the LIFT approach [*Choo et al*., 2004] to increase the signal-to-noise ratio and to filter out the direct wave. LIFT is an amplitude-preserving noise attenuation algorithm composed of a sequence of models applied to data divided in frequency windows and sometimes also to source-receiver offset domains. With this filtering approach, the signal is first modeled, this model is subtracted from the original data, the noise with residual signal is then strongly filtered to extract the residual signal which is then added back to the signal model. In this work, the LIFT was applied in only one frequency window.

5. *Common mid point (CMP) sorting*. Data traces were sorted from the shot gather domain into the CMP domain.

6. *Velocity analysis*. The root-mean-square (RMS) velocities were picked on CMP super

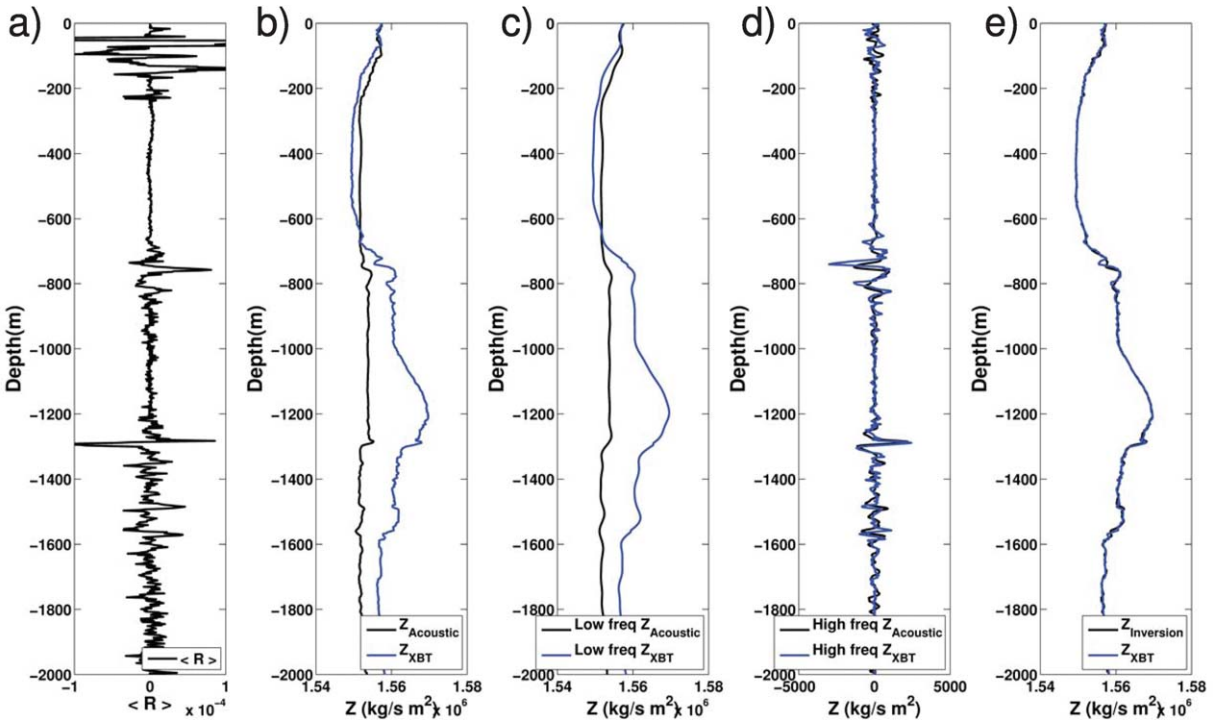

Figure 3. (a) $<R>$ recovered from deconvolution of the acoustic data. (b) Black: Impedance calculated from $<R>$ using equation (7); and blue: impedance calculated from the XBT probe coincident in time and space with the acoustic signal. (c) Low-frequency filter of $Z_{Acoustic}$ (black) and Z_{XBT} (blue). Notice that the low-frequency content of the acoustic impedance does not fit with the oceanographic data. (d) High-frequency filter of $Z_{Acoustic}$ (black) and Z_{XBT} (blue). Notice that the high-frequency content of the acoustic impedance does fit with the oceanographic data. (e) Impedance inversion (black): $Z_{Inversion} = Z_{HighfreqAcoustic} + Z_{LowfreqXBT}$ and XBT impedance (blue).

gathers because the signal-to-noise ratio on stacked sections significantly improves when using velocities derived directly from seismic data instead of that from oceanographic probes [*Fortin and Holbrook*, 2009].

7. *Normal move out* (NMO). Data were NMO-ed to simulate zero-offset data acquisition geometry.

8. *Stack*. Signal arriving from common subsurface locations was summed.

9. *Deconvolution*. Data were deconvolved from the source wavelet by using a minimum entropy filter design algorithm and by extracting the source wavelet from the MCS data through an iterative process. A constant spike decon operator was used with 100 ms length for the whole stacked section.

10. *Migration*. Standard poststack Kirchhoff time migration was applied to the data.

11. *Amplitude calibration*. Calibration with the first multiple method.

3.2. T, S, and ρ Recovery From Reflectivity

The preconditioned data are used as input to the inversion process. First, the impedance is recovered from the extracted zero-offset true-amplitude acoustic reflectivity (R) and the smoothed-background XBT along the MCS profile. Next, temperature and salinity are computed using an empirical T-S relation. Finally, the potential density is computed from T and S. Detailed information on these steps follows:

1. Impedance, referred to as Z from here on, is calculated from R (Figure 3a) using the expression for a continuous medium proposed by [*Oldenburg et al.*, 1983]:

$$<Z_{Acoustic}(i)> = Z(0) * exp\left(2\int_0^{z(i)} <R(z)> dz\right), \quad (7)$$

where $<R(z)>$ is the reflectivity of the medium derived with a band-limited source. The convolutional model only ensures to recover the real reflectivity of the medium if the seismic source is a true delta function. In the real case, when sources are band-limited wavelets, the recovered reflectivity is a part of the real

one, and high and low frequencies outside the source band cannot be well recovered from the seismogram. Therefore, the impedance recovered after deconvolving the acoustic data ($Z_{Acoustic}$) has incorrect low and high-frequency content outside the source frequency band, which must be removed (Figure 3b).

2. $Z_{Acoustic}$ is band-pass filtered $(80\text{Hz} > f > 10\text{Hz})$. The cutoff frequency is chosen based on the frequency band of the source but it is adjusted following trial and error testing. It is important to check the effects on amplitude in every single processing step and recalibrate them by comparing with the XBT information. All the applied frequency filters must be zero-phase filters to preserve the phase of the signal and hence the position of the reflections.

3. The low-frequency information of the impedance is recovered from the XBT data by low-pass filtering with the same cutoff frequency ($f < 10$ Hz) (Figure 3c). Since the XBT data have lower lateral sampling than acoustic data, XBT data must be interpolated after the filtering. The main issue with extracting the low-frequency information from XBTs is that they do not measure salinity, which is needed to calculate the impedance. Unfortunately, although we collected CTD casts that are spatially coincident with the MCS data, they are not temporarily coincident and cannot be used for this process. To solve this problem, a T-S relation for the area of the Gulf of Cadiz was derived using a nonlinear NN-based analysis [*Bishop*, 1995] (supporting information). The application of a NN for T-S relations was first presented by *Ballabrera-Poy et al*. [2009] and was validated for SO applications by *Kormann et al*. [2011].

4. The acoustically derived, high-frequency vertical profiles, and the XBT-derived, low-frequency ones, are summed in the time domain to calculate broadband vertical impedance profiles along the section (Figure 3d).

$$Z_{Inversion} = Z_{HighfreqAcoustic} + Z_{LowfreqXBT} \tag{8}$$

5. T, S, and ρ derivation. Finally, temperature and salinity are assigned from $Z_{Inversion}$ by applying a numerical search that solves for these two unknown variables using the two-equation system:

$$\begin{cases} Z(T,S,p) = \rho(T,S,p) \cdot ss(T,S,p), \\ S = NN(T,p), \end{cases}$$

where $\rho(T,S,p)$ and $ss(T,S,p)$ are the equations provided by the Gibbs Seawater (GSW) Oceanographic Toolbox, for density and sound speed, respectively, and NN(T,p) is the empirical function of salinity derived from temperature and pressure using neural networks.

Finally, the comparison between two strategies for temperature and salinity recovery from reflectivity is presented: the strategy described by *Papenberg et al*. [2010] (strategy 1) and the strategy used in this work (strategy 2). Strategy 1 derives temperature and salinity from sound speed, assuming a depth dependent density profile constant along the whole section and using a linear T-S model, and strategy 2 derives temperature and salinity directly from impedance using a nonlinear T-S model. Strategy 2 does not consider density constant along the profile, either in vertical or lateral dimension and allows eventually the recovery of density from the inverted temperature and salinity. T-S models were trained using the CTD data acquired by the FS Poseidon during the GO survey and the errors of both strategies are calculated by the mean differences between the predictions of both strategies and the CTD data acquired by the RSS Discovery during the GO survey. The description of the T-S linear and nonlinear models used in the comparison can be found in the supporting information of this paper. The differences between the CTD data and the results following the strategy 1 (red curves) and the strategy 2 (black curves) are plotted in Figure 4. Strategy 1 performs better in the shallowest 500 m for all three variables, as well as for temperature in the depth range from 1500 to 2000 m. However, strategy 2 yields significantly better results for the depth range from 500 to 1500 m for the three variables with the errors in the salinity and potential density recovery up to four times smaller than for strategy 1. Strategy 2 also performs better in determining salinity and potential density for the depth range from 1500 to 2000 m.

4. Results

The processing sequence described in the previous section was applied to 2520 shots, resulting in 13,200 1-D vertical acoustic reflection profiles along 82.5 km (Figure 5a). Results of the inversion are 2-D maps of

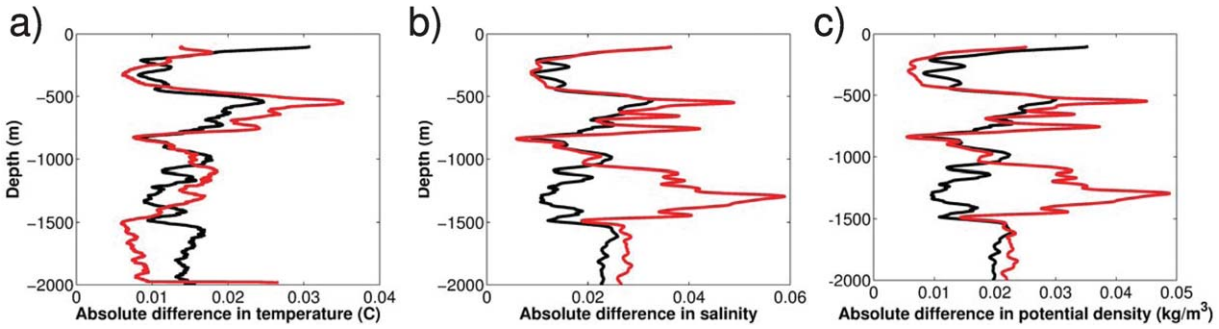

Figure 4. Average absolute differences between CTD data and results from strategy 1 (red) and strategy 2 (black) for: (a) temperature, (b) salinity, and (c) potential density.

temperature, salinity, and potential density, which cover the water column at depths from 100 to 1800 m and have a vertical resolution of ~10 m and a lateral resolution of ~100 m (Figures 5b–5d). The lateral resolution is of the order of the width of the first Fresnel zone, $\sqrt{(\lambda d/2)}$ [*Yilmaz*, 2001], which is affected by the

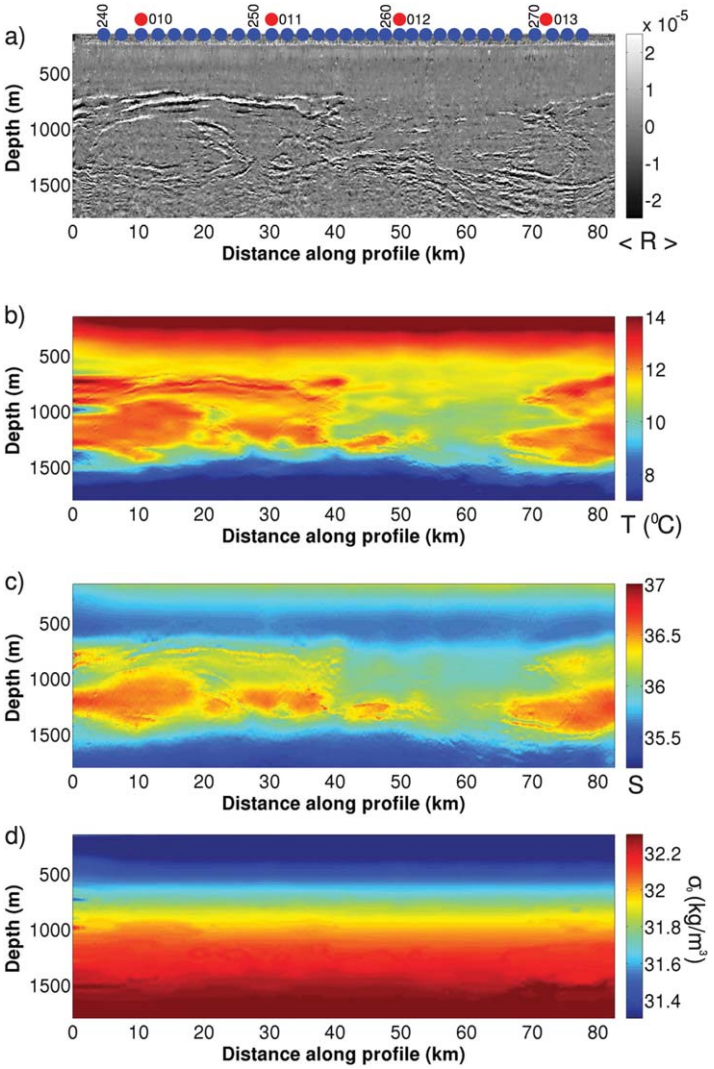

Figure 5. (a) Acoustic reflections in the profile GOLR10, Gulf of Cadiz, Northwestern Atlantic Ocean, 1 May 2007. Red dots show the location of the CTD probes and blue dots show the location of the XBT probes. Inversion results of (b) temperature, (c) salinity, and (d) potential density anomaly.

distance between the source and the reflector (in our data distances range between 100 and 1800 m), and the dominant wavelength of the source, $\lambda = 30$ m. We did not invert data shallower than 100 m because of the direct wave, which is the wave that travels directly from the acoustic source to the receivers without reflecting. This wave, which is characterized by strong amplitudes (10^4 times larger than for the water layer reflections), overprints and distorts the signal in the shallowest layer and is difficult to completely suppress while preserving the amplitude of the reflections. Therefore, the starting point of equation (7) was $Z(0) = Z_{XBT}(Z = 100\text{m})$ and the mixed layer was out of the scope of this work.

The inverted profiles show a warm and salty water mass of MW occupying the 500–1500 m deep layer of the Gulf of Cadiz basin and are surrounded by fresh and cold NAIW above and NADW below (Figure 5). The MU is tracked at the right side of the profile, adjacent to the continental slope. Two MU cores can be identified at depths of 800 and 1200 m. From 3 to 10 km and at depth from 800 to 1200 m, there is a warm and salty lens that we interpret as a meddy. From 35 to 40 km in the profile, 20 km far away from the lateral right edge of the meddy there is a vertical thermohaline anomaly that is similar to the spiral arm of a meddy described by *Ménesguen et al*. [2012].

The coincident oceanographic probes were used to obtain the $Z_{LowfreqXBT}$ model and also for the error analysis. We inverted the acoustic reflectivity with the $Z_{LowfreqXBT}$ model including all the XBTs with a lateral spacing of 2.5 km. We then calculated the differences between XBT data and inversion results and the mean standard deviations of the whole acoustic profile are $\delta T_{sd} = 0.09°\text{C}$, $\delta S_{sd} = 0.02$, and $\delta \rho_{sd} = 0.004\text{kg/m}^3$ (Figure 6). In addition, we repeated all the inversions but excluded every other XBT of the $Z_{LowfreqXBT}$ model and then we recalculated the standard deviations. These errors represent the errors at the location where XBT smoothed profiles were removed. In this case, the $Z_{LowfreqXBT}$ model had a lateral resolution of 5 km instead of 2.5 km and the corresponding differences are $\delta T_{sd} = 0.3°\text{C}$, $\delta S_{sd} = 0.07$, and $\delta \rho_{sd} = 0.01\text{kg/m}^3$, which are more than twofold the first computed errors. Our results show that the quality of $Z_{LowfreqXBT}$ in this case determines the main uncertainty of the inversion. Since our acoustic source does not allow the recovery of $Z_{Acoustic}$ in frequencies lower than 10 Hz, we have to obtain the mesoscale information from the XBTs and therefore the lateral sampling of these probes significantly affects the quality of the inversion. Finally, we compared the inversions with the spatially coincident CTD profiles (Figure 7). CTD probes were not included in the inversion and they were not coincident in time, with a difference of 2–3 h of the acoustic acquisition. The standard deviations of the four CTDs are $\delta T_{sd} = 0.3°\text{C}$, $\delta S_{sd} = 0.09$, and $\delta \rho_{sd} = 0.02\text{kg/m}^3$. Since the CTD values of salinity and potential density are independent of the T-S relation, we consider the differences between these CTD values and the inverted ones as the salinity and potential density errors of our method. Therefore, the errors of T, S, and ρ inversions are $\delta T_{sd} = 0.1°\text{C}$ (from XBT comparison), $\delta S_{sd} = 0.09$ (from CTD comparison), and $\delta \rho_{sd} = 0.02\text{kg/m}^3$ (from CTD comparison). The T and S fluctuations are highly correlated and nearly density-compensating, so that the inferred density has relatively larger errors than T or S alone. Unrealistic potential density inversions, smaller than the error bars but too large vertically (~15 m) are observed in the results. To prevent them, the isopycnal contours presented below correspond to the potential density field smooth over 50 m in the vertical dimension. The results obtained in the left side of the profile, between 0 and 3 km, were distorted by the lateral extrapolation of the $Z_{LowfreqXBT}$ model, so they are not considered in the further analysis.

Temperature anomaly was calculated by subtracting a mean value from the inverted results, $T_{Anom} = T_{Inv} - T_0$, with $T_0 = 9.88°\text{C}$ (mean value of a vertical profile placed at 60 km of GOLR01). T_{Anom} (Figure 8) show intrusions developed at baroclinic thermohaline fronts placed at the Mediterranean tongue level. The fronts present strongly compensated thermohaline intrusions with weak signature in density. The clearest filaments are located in lateral T-S gradients: (a) at the lateral edge of the lens, between 19.5 and 21.5 km and from 980 to 1080 m deep; (b) at the upper core of the MU, between 66 and 71 km and from 840 to 940 m deep; and (c) at the spiral arm of the lens, between 42 and 54 km and 700–900 m deep and between 1040 and 1140 m deep. The filaments have widths of: (a) 500 m, (b) 1 km; and (c) 6 km and 2 km and thicknesses of (a) 20 m, (b) 20 m; and (c) 100 m and 50 m, which agree with previous descriptions of tracer simulated filaments in T-S lateral gradients in this area [*Smith and Ferrari*, 2009]. These filaments are zoomed and overlapped with contours of inverted potential density every 0.02 kg/m^3. The filaments at (a) and (b) are multiple and have small slopes with respect to isopycnals, while the tendrils at (c) are individual and have slopes (inverse of the aspect ratio) of 0.008 rad (filament at ~780 m depth) and 0.03 rad (filament at ~1080 m depth) with respect to the isopycnals.

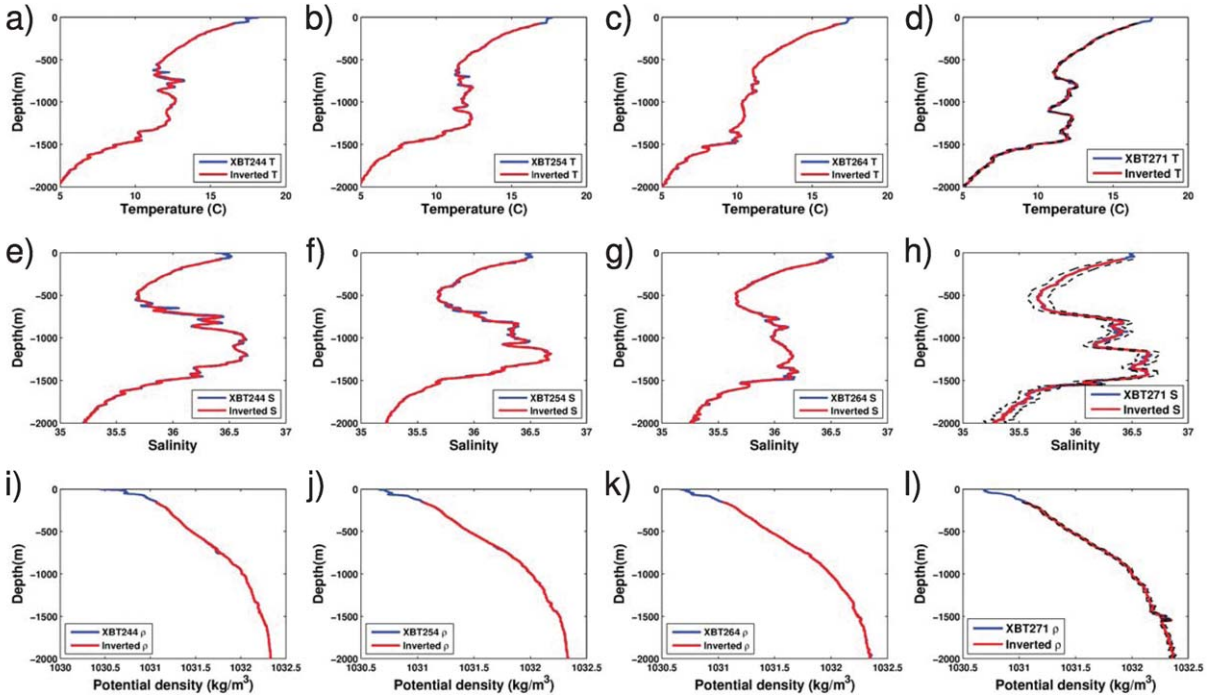

Figure 6. Time and space coincident XBT data and results from the inversion of acoustic data showing: temperature at (a) XBT 244, (b) XBT 254, (c) XBT 264, and (d)XBT 271; salinity at (e) XBT 244, (f) XBT 254, (g) XBT 264, and (h) XBT 271; and potential density at (i) XBT 244, (j) XBT 254, (k) XBT 264, and (l) XBT 271. Black curves show the error range of the method.

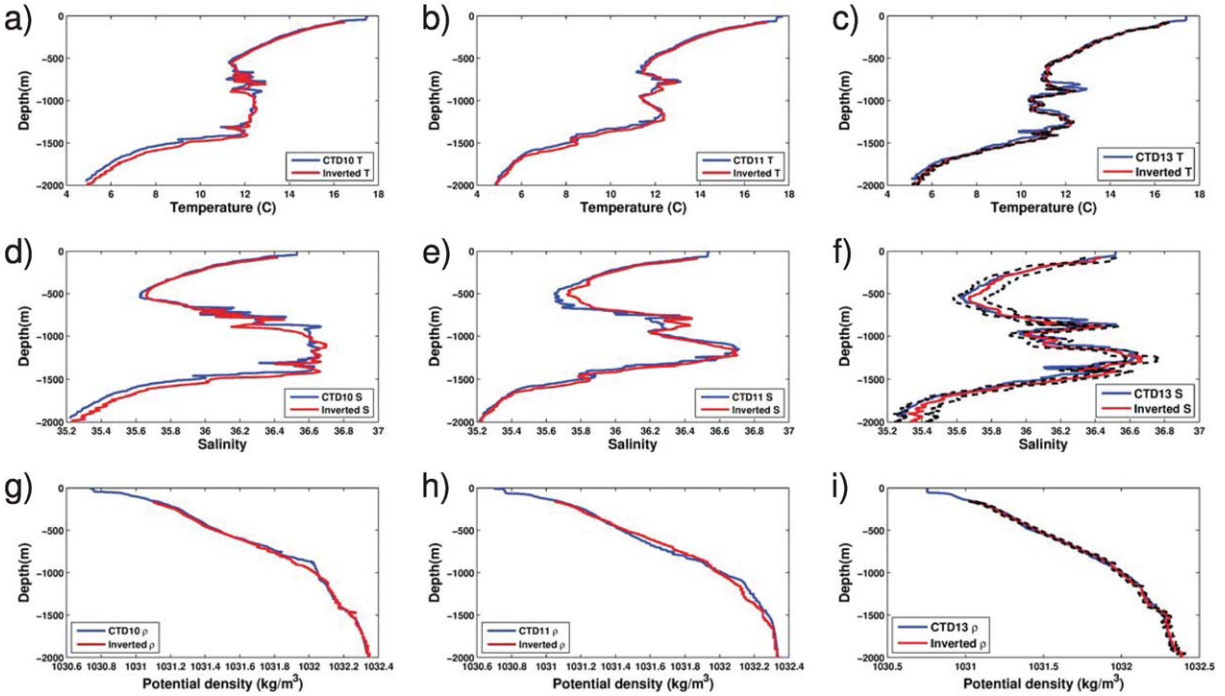

Figure 7. Space-coincident CTD data and results from the inversion of acoustic data showing: temperature at (a) CTD 010, (b) CTD 011, and (c) CTD 013; salinity at (d) CTD 010, (e) CTD 011, and (f) CTD 012 and potential density at (g) CTD 010, (h) CTD 011, and (i) CTD 012. Black curves show the error range of the method.

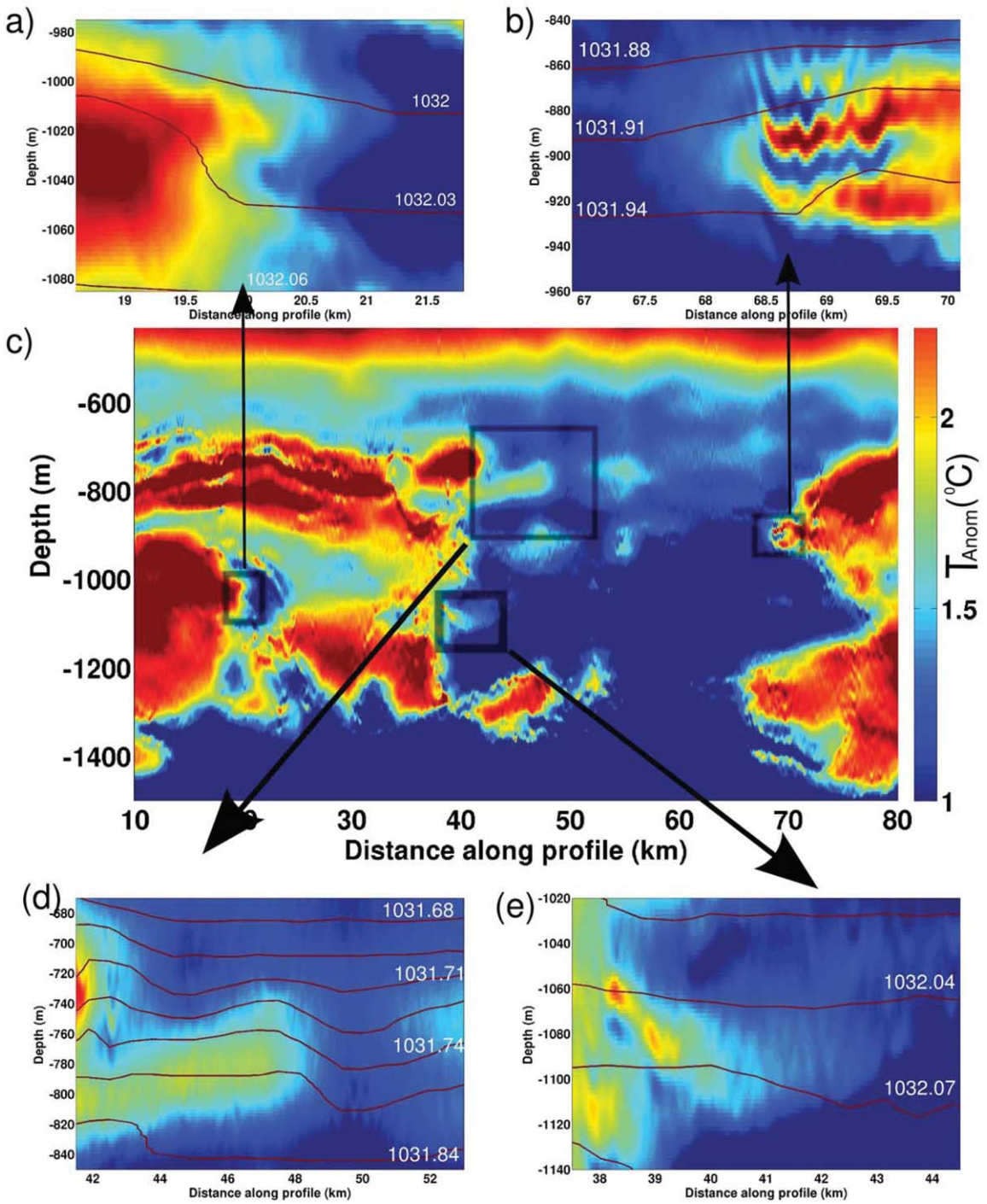

Figure 8. Inverted temperature anomalies of the GOLR01 profile, Gulf of Cadiz, North Atlantic Ocean, 1 May 2007. The filaments described in the text are zoomed at (a) the lateral edge of the meddy, (b) the upper core of the MU, and (d and e) the thermohaline front at 35–40 km of the profile. The thermal anomalies of the whole profile are shown in Figure 8c. Isopycnal contours are plotted every 0.03 kg/m^3.

4.1. Potential Density

Although the contribution of the density contrast to the reflectivity in the ocean is significantly smaller than the contribution of the sound speed contrast as quantified by *Sallarès et al.* [2009], our results show that this variable can be inverted from acoustic reflectivity with an accuracy of $\delta\rho_{sd}=0.02\mathrm{kg/m}^3$.

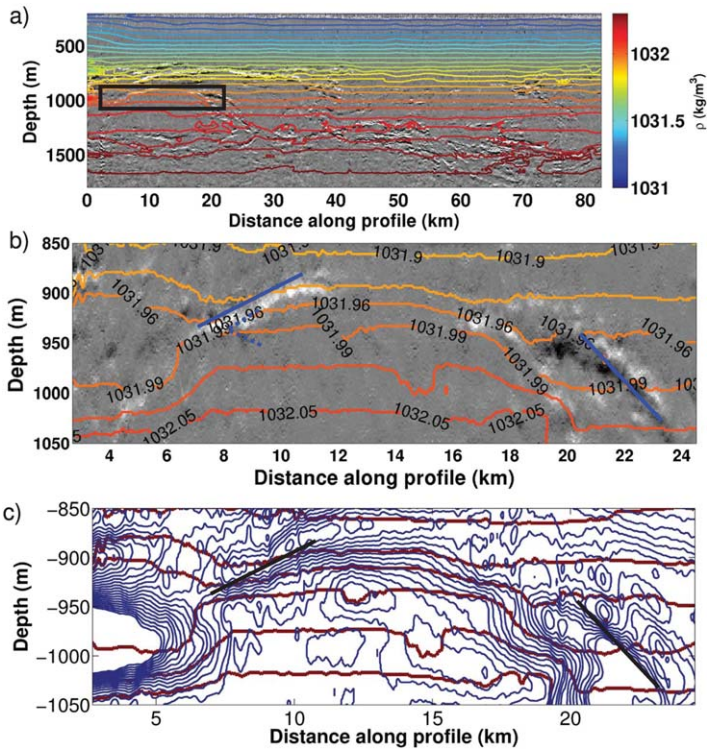

Figure 9. (a) Inverted isopycnal contours overlapped with acoustic reflectivity in GOLR01 profile, Gulf of Cadiz, North Atlantic Ocean, 1 May 2007. (b) Zoom of the square in top image. (c) Inverted isopycnals (dark red) and thermal contours (blue) of the zoom in Figure 9b. Isopycnal contours are plotted every 0.02 kg/m^3 and thermal contours are plotted every 0.2°C. Solid straight blue lines follow the continuous reflector and dashed blue lines indicate the potential density error in the inversion.

Reflectivity has been interpreted as isopycnal surfaces in recent SO works [*Krahmann et al*., 2008; *Sheen et al*., 2013; *Holbrook et al*., 2013]. We compare the inverted potential density contours, i.e., isopycnal surfaces, with the acoustic reflectivity data in Figure 9. These comparisons show that acoustic reflectors are not isopycnal in all domains. If we follow the continuous reflectors on the top boundary of the meddy (Figure 9b), the value of potential density changes along the reflector, even considering the range of error $(\pm 0.02 \mathrm{kg/m^3})$. The slope of the isopycnal is similar to the reflector along a limit distance (less than $\sim 1-2$ km in the lateral and 20–50 m in the vertical in our data), while the thermal gradients completely overlap the continuous reflector (Figure 9c).

5. Discussion and Conclusions

Temperature anomalies (Figure 8) calculated from the inverted data show intrusions in areas with lateral T-S gradients. These areas present baroclinic thermohaline fronts with filaments of thicknesses on the order of 10 m and widths that range between hundreds of meters and tens of kilometers and strong T-S lateral compensations. At least two main theories have been proposed to explain the generation of thermohaline structures with weak density signature below the surface mixed layer. The first explained by *Ruddick and Gargett* [2003] states that lateral T-S gradients drive double-diffusive intrusions that are developed along isopycnals. The second states that the large T-S anomalies are stirred along isopycnals by mesoscale eddies, creating filaments with typical slopes of f/N [*Smith and Ferrari*, 2009]. Two of the four areas selected in our data, at the lateral edge of the meddy and at the MU upper core, show multiple near-isopycnal filaments, which agree with the double-diffusive theory. In the front created by the spiral arm and the surrounded MW, the filaments do not follow isopycnals. The slope of the upper filament is 0.008 rad, in this area the buoyancy frequency $\left(N=\sqrt{-\frac{g\frac{d\rho}{dz}}{\rho_0}}\right)$ is $2.7\times10^{-3}\pm8\times10^{-4}$ and the Coriolis parameter (f) is 0.85×10^{-4}, so $f/N=3\times10^{-2}\pm9\times10^{-3}$, which is an order of magnitude bigger than the slope of the filament. However,

the lower tendril has a slope of 0.03 rad and in this area f/N is also $3\times10^{-2}\pm9\times10^{-3}$, which agrees with the stirring theory. Note that ideally 3-D data should be used for a further discussion on that topic, since the slopes observed by our method are limited by the angle between the acoustic profile and the filaments.

Previous works on SO have assumed that acoustic reflectors follow isopycnals surfaces, mainly concerning two different topics, the study of the energy cascading from internal waves to turbulence done in *Krahmann et al*. [2008], *Sheen et al*. [2009], *Holbrook et al*. [2013], and the interpretation of dynamics of the Sub-Antarctic Front done by *Sheen et al*. [2013]. Since acoustic impedance is a product of density and sound speed, contrasts in density must generate contrasts in impedance and hence reflectivity and, at the same time, contrasts in sound speed generate reflectivity as well. However, because of the strong correlation between temperature and salinity observed in the ocean [*Rudnick and Ferrari*, 1999], thermal contrasts can be compensated by haline contrasts minimizing density changes. Therefore, strong vertical contrasts in sound speed can have low contrasts in density and potential density. Previous works [*Nandi et al*., 2004; *Ruddick et al*., 2009] explain that acoustic reflections are primarily associated with temperature vertical variations, so acoustic images in the ocean can be interpreted as maps of thermal gradients, in agreement with the results presented in this work (Figure 9). On the contrary, isopycnals cross acoustic reflectors and thermal contours in areas of lateral thermal and haline compensation.

To confirm this observation and link this result with previous SO works, we have modeled two synthetic domains in Figure 10. We have constructed two temperature models ($T_1=10.2^\circ$C and $T_2=10^\circ$C) for predominantly: (a) lateral and (b) vertical thermal variations. Using an empirical T-S relation, we have obtained the corresponding synthetic models for density and sound speed and we have propagated a synthetic acoustic wave using the 1-D acoustic propagation solver of *Bornstein et al*. [2013]. In the same figure, we plot the reflectivity and isopycnal contours derived from both models. In the lateral thermal gradient, isopycnals vary along the continuous reflector (Figure 10c), while in the vertical thermal stratification the isopycnal follows the thermal interface (Figure 10d). These results highlight that the hypothesis of considering acoustic reflectivity as a proxy of isopycnal surfaces is not valid for all the dynamic domains, but it is case-by-case dependent, and it is specially weak in the case of lateral interleaving or fronts, while the studies of internal wave energy from undulating reflectors within a vertical thermal gradient should be valid.

In potential density analysis, the T-S relation plays a key role. We have used the NN T-S relation in all this work because it gives the best results for the whole water column, from surface up to 2000 m deep, and within the different submesoscale structures that we have in our data set (i.e., Mediterranean Undercurrent and meddies) (supporting information). However, we note that the error in potential density inversion can significantly increase depending on the used T-S relation that is used. Because of that, we consider that the synthetic FWI inversion presented by *Bornstein et al*. [2013] is very promising since they do not use any T-S relation and invert independently temperature and salinity directly from the acoustic wave minimizing the error in potential density. As a final test, we have applied the method of *Bornstein et al*. [2013] to invert potential density from the synthetic reflectivity along a section of a meddy. The result, which is shown in Figure 11, corroborates that potential density varies along the continuous reflector of the top of the core and hence reflectivity is not isopycnal.

In summary, this work shows that the main physical oceanographic parameters in the ocean: temperature, salinity, and potential density, can be inverted from acoustic reflectivity with accuracies of $\delta T_{sd}=0.1^\circ$C, $\delta S_{sd}=0.09$, and $\delta\rho_{sd}=0.02\mathrm{kg/m}^3$ for temperature, salinity, and potential density, respectively. There is no need to assume laterally homogeneous density during the inversion and T and S variables can be inverted directly from impedance. For acoustic sources with frequency content above 10 Hz, XBTs coincident in time and space to the acoustic data acquisition are needed for the inversion. A lateral sampling of 2.5 km for the coincident XBTs is suggested for inversions in the Gulf of Cadiz, where high lateral submesoscale variability is observed. XBTs also play a key role in the calibration of the inversion amplitudes. The observations support a mix of reflective features created by both double-diffusive and isopycnal stirring mechanisms. Our results show that reflectivity follows thermal gradients but acoustic reflectors may have potential density variations along them, specially when fronts are present.

In several scientific fields such as medicine, astronomy, geology, etc., the exploration using waves has significantly improved the observation. Because of the magnitude, variability, and inaccessibility of the ocean, we believe that methods based on acoustic observations should be further developed and better adapted to

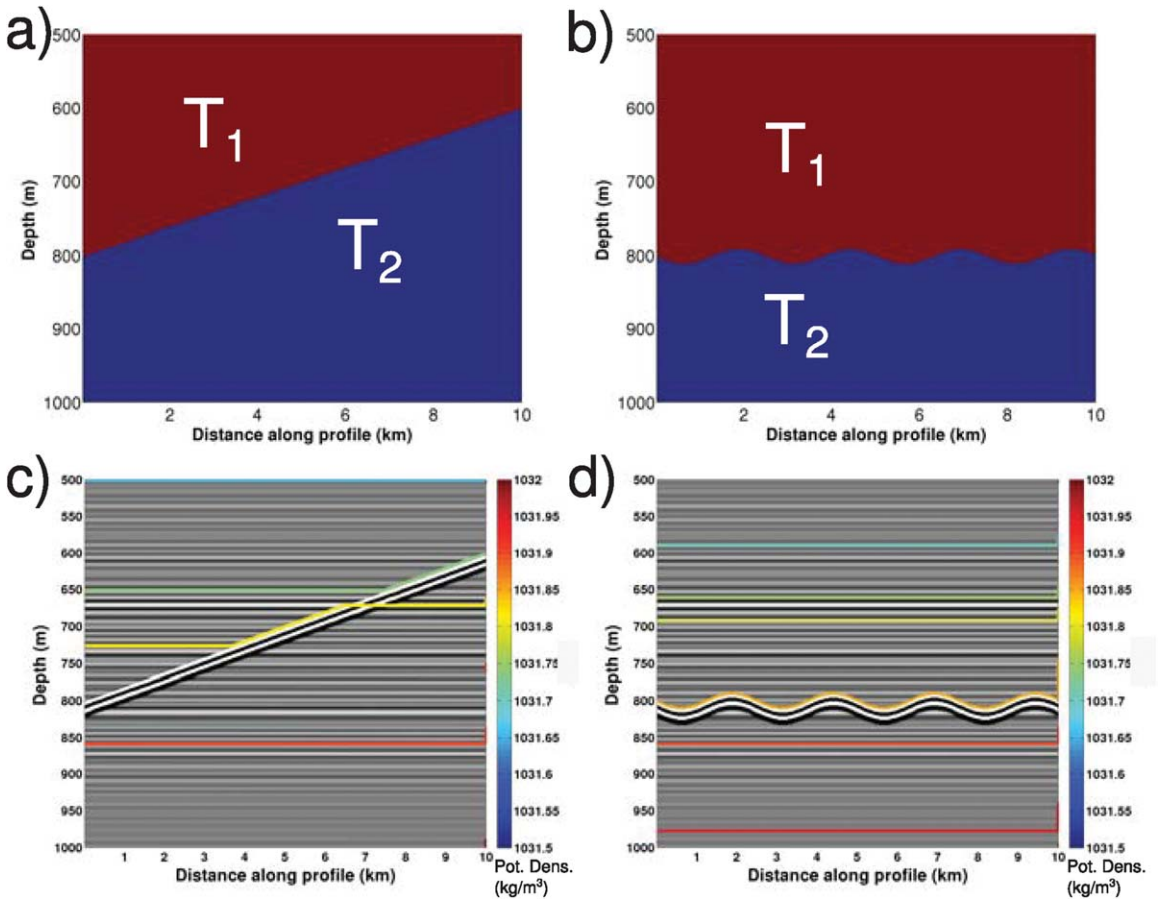

Figure 10. Synthetic models of two temperatures $T_1 = 10.2°C$ and $T_2 = 10°C$ with (a) predominantly lateral gradient and (b) predominantly vertical gradient. (c) Synthetic acoustic reflectivity and isopycnals of model Figure 10a. (d) Synthetic acoustic reflectivity and isopycnals of model Figure 10b. Colored contours correspond to potential density values.

the physical oceanography. SO has proven that reflectivity can give information to interpret the main physical parameters. However, the MCS instrumentation that is used at the present time is not optimally adapted to the ocean, which decreases the potential of this acoustic method in oceanographic research. One remarkable limit is the exploration of the mixed layer, with high climatic importance because of the coupling with the atmosphere. Alternatives for shallow SO instrumentation have been presented in *Piètè et al.* [2013], but a general solution is still missing. An effort should be made to adapt the principles and technology of MCS system to oceanic exploration. The key points to be assessed include the use of acoustic sources broader in frequency content and more portable acquisition systems to be installed in midsize oceanographic vessels.

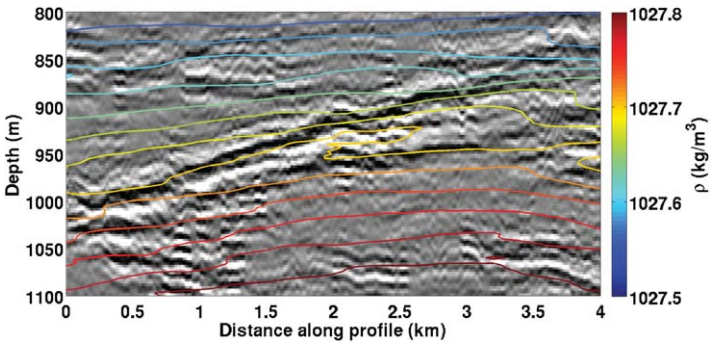

Figure 11. Isopycnal contours inverted using the FWI method from synthetic seismic data [*Bornstein et al.*, 2013].

Acknowledgments
The first author is funded by a Marie Curie IOF Fellowship (EU) with the project FP7-PEOPLE-2010-IOF-271936-OCEANSEIS. This work was also supported by the project POSEIDON (CTM2010-25169) and complementary action APOGEO (CTM2011-16001-E) from the Spanish Ministry MINECO. We want to thank the three anonymous reviewers for their detailed corrections and suggestions, which have helped us to significantly improve the manuscript. The data of this paper were acquired in the GO project (EU-NEST2003-15603) and can be requested at http://www.utm.csic.es/so/contact.

References

Ambar, I., N. Serra, M. Brogueira, G. Cabeçadas, F. Abrantes, P. Freitas, C. Gonçalves, and N. González (2002), Physical, chemical and sedimetological aspects of the Mediterranean outflow off Iberia, *Deep Sea Res., Part II*, *49*, 4163–4177.

Armi, L., D. Herbert, N. Oakey, J. Price, P. Richardson, H. Rossby, and B. Ruddick (1989), Two years in the life of a Mediterranean salt lens, *J. Phys. Oceanogr.*, *19*, 354–370.

Ballabrera-Poy, J., B. Mourre, E. García-Ladona, A. Turiel, and J. Font (2009), Linear and non-linear t-s models for the eastern North Atlantic from Argo data: Role of surface salinity observations, *Deep Sea Res., Part I*, *56*, 1605–1614.

Biescas, B., V. Sallarès, J. Pelegrí, F. Machín, R. Carbonell, G. Buffett, J. Dañobeitia, and A. Calahorrano (2008), Imaging meddy finestructure using multichannel seismic reflection data, *Geophys. Res. Lett.*, *35*, L11609, doi:10.1029/2008GL033971.

Biescas, B., L. Armi, V. Sallarès, and E. Gràcia (2010), Seismic imaging of staircase layers below the Mediterranean undercurrent, *Deep Sea Res., Part I*, *57*, 1345–1353, doi:10.1016/j.dsr.2010.07.001.

Bishop, C. (1995), *Neural Network for Pattern Recognition*, Oxford Univ. Press, N. Y.

Bornstein, G., B. Biescas, A. Sallares, V. Bower, and J. Mojica (2013), Direct temperature and salinity acoustic full waveform inversion, *Geophys. Res. Lett.*, *40*, 4344–4348, doi:10.1002/grl.50844.

Bower, A., N. Serra, and I. Ambar (2002), Structure of Mediterranean undercurrent and Mediterranean water spreading around the southwestern Iberian Peninsula, *J. Geophys. Res.*, *107*(C10), 3161, doi:10.1029/2001JC001007.

Buffett, G., B. Biescas, J. Pelegrí, F. Machín, V. Sallarès, R. Carbonell, D. Klaeschen, and R. Hobbs (2009), Seismic reflection along the path of the Mediterranean undercurrent, *Cont. Shelf Res.*, *29*, 1848–1860.

Choo, J., J. Downton, and D. J. (2004), Lift: A new and practical approach to noise and multiple attenuation, *First Break*, *22*, 39–44.

Ferrari, R., and K. Polzin (2005), Finescale structure of the t-s relation in the eastern north Atlantic, *J. Phys. Oceanogr.*, *35*, 1437–1454.

Fortin, W., and W. Holbrook (2009), Sound speed requirements for optimal imaging of seismic oceanography data, *Geophys. Res. Lett.*, *36*, L00D01, doi:10.1029/2009GL038991.

Gonella, J., and D. Michon (1988), Ondes internes profondes révélées par sismique réflexion au sein des masses d'eua en atlantique-est, *C. R. Acad. Sci., Ser. II*, *306*, 781–787.

Holbrook, W., P. Páramo, S. Pearse, and W. Schmitt (2003), Thermohaline fine structure in an oceanographic front from seismic reflection profiling, *Science*, *301*, 821–824.

Holbrook, W., I. Fer, W. Schmitt, D. Lizarralde, J. Klymak, C. Helfrich, and R. Kubichek (2013), Estimating oceanic turbulence dissipation from seismic images, *J. Atmos. Oceanic Technol.*, *30*, 1767–1788, doi:10.1175/JTECH-D-12-00140.1.

Kormann, J., B. Biescas, N. Korta, J. de la Puente, and V. Sallarès (2011), Application of acoustic full waveform inversion to retrieve high-resolution temperature and salinity profiles from synthetic seismic data, *J. Geophys. Res.*, *116*, C11039, doi:10.1029/2011JC007216.

Krahmann, G., P. Brandt, D. Klaeschen, and T. Reston (2008), Mid-depth internal wave energy off the Iberian Peninsula estimated from seismic reflection data, *J. Geophys. Res.*, *113*, C12016, doi:10.1029/2007JC004678.

Ménesguen, C., B. Hua, X. Carton, F. Klingelhoefer, P. Schnurle, and C. Reichert (2012), Arms winding around a meddy seen in seismic reflection data close to the morocco coastline, *Geophys. Res. Lett.*, *39*, L05604, doi:10.1029/2011GL050798.

Nandi, P., W. Holbrook, S. Pearse, P. Páramo, and R. Schmitt (2004), Seismic reflection imaging of water mass boundaries in the Norwegian Sea, *Geophys. Res. Lett.*, *31*, L23311, doi:10.1029/2004GL021325.

Oldenburg, D., T. Scheuer, and S. Levy (1983), Recovery of the acoustic impedance from reflection seismograms, *Geophysics*, *48*, 1318–1337.

Papenberg, C., D. Klaeschen, G. Krahmann, and R. Hobbs (2010), Ocean temperature and salinity inverted from combined hydrographic and seismic data, *Geophys. Res. Lett.*, *37*, L04601, doi:10.1029/2010GL042115.

Piètè, H., L. Marié, B. Marsset, Y. Thomas, and M. Gutscher (2013), Seismic reflection imaging of shallow oceanographic structures, *J. Geophys. Res. Oceans*, *118*, 2329–2344, doi:10.1002/jgrc.20156.

Richardson, P., A. Bower, and W. Zenk (2000), A census of Meddies tracked by floats, *Prog. Oceanogr.*, *45*, 209–250.

Rudnick, D., and R. Ferrari (1999), Compensation of horizontal temperature and salinity gradients in the ocean mixed layer, *Science*, *283*, 526–529, doi:10.1126/science.283.5401.526.

Ruddick, B., and A. Gargett (2003), Oceanic double-infusion: Introduction, *Prog. Oceanogr.*, *56*(3–4), 381–393.

Ruddick, B., and K. Richards (2003), Oceanic thermohaline intrusions: Observations, *Prog. Oceanogr.*, *56*(3–4), 499–527.

Ruddick, B., H. Song, C. Dong, and L. Pinheiro (2009), Water column seismic images as maps of temperature gradient, *Oceanography*, *22*(1), 193–205.

Sallarès, V., B. Biescas, G. Buffett, R. Carbonell, J. Dañobeitia, and J. Pelegrí (2009), Relative contribution of temperature and salinity to ocean acoustic reflectivity, *Geophys. Res. Lett.*, *36*, L00D06, doi:10.1029/2009GL040187.

Serra, N., and I. Ambar (2005), Observations and numerical modelling of the Mediterranean outflow splitting and eddy generation, *Deep Sea Res., Part II*, *52*, 383–408.

Sheen, K., N. White, and R. Hobbs (2009), Estimating mixing rates from seismic images oceanic structures, *Geophys. Res. Lett.*, *36*, L00D04, doi:10.1029/2009GL040106.

Sheen, K., N. White, C. Caulfiel, and R. Hobbs (2013), Seismic imaging of a large horizontal vortex at abyssal depths beneath the Sub-Antarctic front, *Nat. Geosci.*, *5*, 542–546, doi:10.1038/NGEO1502.

Sheriff, R., and L. Geldart (1982), *Exploration Seismology: History, Theory and Data Acquisition*, vol. 1, 253 pp., Cambridge Univ. Press, Cambridge, U. K.

Smith, K., and R. Ferrari (2009), The production and dissipation of compensated thermohaline variance by mesoscale stirring, *J. Phys. Oceanogr.*, *39*, 2477–2501.

Tait, R., and M. Howe (1968), Some observations of thermo-haline stratification in the deep ocean, *Deep Sea Res. Oceanogr. Abstr.*, *15*, 275–280.

Wood, W., W. Holbrook, M. Sen, and P. Stoffa (2008), Full waveform inversion of reflection seismic data for ocean temperature profiles, *Geophys. Res. Lett.*, *35*, L04608, doi:10.1029/2007GL032359.

Yilmaz, O. (2001), *Seismic Data Analysis: Processing, Inversion, and Interpretation of Seismic Data*, 2nd ed., 2027 pp., Soc. of Explor. Geophys., Tulsa, Okla.